

Contents lists available at ScienceDirect

Earth and Planetary Science Letters

www.elsevier.com/locate/epsl



Shock impedance amplified impact deformation of zircon in granitic rocks from the Chicxulub impact crater



Axel Wittmann ^{a,*}, Aaron J. Cavosie ^b, Nicholas E. Timms ^b, Ludovic Ferrière ^c, Auriol Rae ^{d,e}, Cornelia Rasmussen ^{f,g}, Catherine Ross ^{f,g}, Daniel Stockli ^g, Martin Schmieder ^{h,i}, David A. Kring ⁱ, Jiawei Zhao ^j, Long Xiao ^{j,k}, Joanna V. Morgan ^l, Sean P.S. Gulick ^{f,g,m} and the IODP-ICDP Expedition 364 Scientists

- ^a Eyring Materials Center, Arizona State University, 1001 S. McAllister Avenue, Tempe, AZ 85287-8301, USA
- b Space Science and Technology Centre, School of Earth and Planetary Sciences, Curtin University, Perth, GPO Box U1987, Western Australia 6845, Australia
- ^c Natural History Museum, Burgring 7, 1010 Vienna, Austria
- d Institute of Earth and Environmental Sciences Geology, Albert-Ludwigs Universität Freiburg, Freiburg, Germany
- ^e Department of Earth Sciences, University of Cambridge, Cambridge, UK
- f Institute for Geophysics, Jackson School of Geosciences, University of Texas at Austin, TX 78758-4445, USA
- g Department of Geological Sciences, Jackson School of Geosciences, University of Texas at Austin, 22275 Speedway Stop C9000 Austin, TX 78712, USA
- ^h HNU Neu-Ulm University of Applied Sciences, Neu-Ulm, Germany
- ⁱ Lunar and Planetary Institute, Houston, TX, USA
- j State Key Laboratory of Geological Processes and Mineral Resources, Planetary Science Institute, School of Earth Sciences, China University of Geosciences, Wuhan, China
- k Chinese Academy of Sciences Center for Excellence in Comparative Planetology, Hefei, 230026, China
- ¹ Department of Earth Science and Engineering, Imperial College London, UK
- ^m Center for Planetary Systems Habitability, University of Texas at Austin, Austin, TX, USA

ARTICLE INFO

Article history: Received 23 March 2021 Received in revised form 25 August 2021 Accepted 6 September 2021 Available online xxxx Editor: W.B. McKinnon

Keywords: zircon reidite Chicxulub peak ring shock impedance

ABSTRACT

Zircon is a precise chronometer and prominent recorder of impact deformation. However, many impactinduced features in zircon are poorly calibrated, sometimes due to contradicting experimental data, in other instances due to the lack of systematic studies of impact-deformed zircon. To resolve issues with the shock petrographic use of zircon, we classified impact deformation features in 429 zircon grains in a continuous drill core of uplifted, granitic bedrock in the peak ring of the 200-km-diameter K-Pg Chicxulub impact structure. Following initial identification in backscattered electron (BSE) images, Raman spectroscopy and electron backscatter diffraction confirmed one reidite-bearing zircon grain. Quartzbased shock barometry indicates the host rock of this zircon-reidite grain experienced an average shock pressure of 17.5 GPa. A survey of BSE images of 429 ZrSiO₄ grains found brittle deformation features are ubiquitous, with planar fractures in one to five sets occurring in 23% of all zircon grains. Our survey also reveals a statistically significant correlation of the occurrence of planar fractures in zircon with the types of host materials. Compared to zircon enclosed in mafic, higher density mineral hosts, felsic, low-density minerals show a much higher incidence of zircon with planar fractures. This finding suggests amplification of pressure due to shock impedance contrasts between zircon and its mineral hosts. Using the impedance matching method, we modeled the shock impedance pressure amplification effect for zircon inclusions in Chicxulub granitic hosts. Our modeling indicates shock impedance could have amplified the average 17.5 GPa shock pressure in a zircon inclusion in quartz or feldspar in the Chicxulub granitic rocks to 24 \pm 1 GPa, suggesting that reidite in these rocks formed between 17.5 and 25 GPa. In essence, our study of impedance-induced shock pressure amplification in zircon assemblages, including the onset of reidite formation, details how shock impedance in mineral associations can be quantified to refine shock pressure estimates.

© 2021 The Author(s). Published by Elsevier B.V. This is an open access article under the CC BY license (http://creativecommons.org/licenses/by/4.0/).

^{*} Corresponding author.

1. Introduction

1.1. Impact petrologic significance of zircon

Zircon ($ZrSiO_4$) is a precise geochronometer and can be used for determining accurate impact ages (e.g., Kenny et al., 2017; Rasmussen et al., 2019). In addition, ZrSiO₄ records a wide variety of impact-induced deformation features such as microtwins, planar fractures, and decomposition to ZrO₂ + SiO₂, spanning pressures between ~ 10 and ~ 90 GPa, and temperatures > 2370 °C (Mashimo et al., 1983; Kusaba et al., 1985; Moser et al., 2011; Erickson et al., 2017; Timms et al., 2017a, 2017b; Cavosie et al., 2018). Among its most intriguing properties is the transformation to the quenchable high-pressure polymorph reidite (e.g., Glass et al., 2002). The onset of the transition of zircon to reidite has been reported from static multi-anvil pressure experiments and shortduration, dynamic shock recovery experiments between 18 and 30 GPa at ambient temperatures (van Westrenen et al., 2004; Morozova et al., 2018; Kusaba et al., 1985; Fiske et al., 1994; Leroux et al., 1999; Erickson et al., 2020). Reidite is increasingly recognized as a component of allochthonous terrestrial and extraterrestrial impactites (e.g., Timms et al., 2017a; Chen et al., 2019; Xing et al., 2020), but it has seldom been detected in parautochthonous settings with intact lithologic contexts that allow the reconstruction of the impact metamorphic conditions for the formation and preservation of reidite (Cox et al., 2018).

1.2. The Chicxulub impact structure

The K-Pg Chicxulub impact produced a ca. 200 km-diameter crater with a global ejecta layer and terminated the Mesozoic Era (e.g. Morgan et al., 2017, and references therein). The crater was previously drilled onshore but evidence for the preservation of shock-produced high-pressure mineral phases was limited (Lounejeva et al., 2002), possibly due to pervasive alteration and post-shock annealing of impactites (Wittmann et al., 2006). More recently, International Ocean Discovery Program (IODP) - International Continental Scientific Drilling Program (ICDP) Expedition 364 recovered 840 m of drill core at 21 27.009'N, 89 56.962'W from the Chicxulub peak ring, including a continuous section through Paleozoic granitic rocks and associated intrusives (Fig. 1; Morgan et al., 2016, 2017; Zhao et al., 2020). The average shock metamorphic overprint of these parautochthonous granitic rocks is 16 to 18 GPa based on shock features in quartz (Feignon et al., 2020). Furthermore, the high-pressure polymorph srilankite (TiO2-II) also occurs in these granitic rocks, which can form at shock pressures <20 GPa and is stable up to temperatures of 400 °C (Kring et al., 2020, and references therein). Electron backscatter diffraction (EBSD) analyses of 23 zircon crystals in these granitic peak-ring rocks have documented shock-produced planar fractures and rare mechanical twins but not reidite (Timms et al., 2019; Cox et al., 2020; Zhao et al., 2021), which, however, does occur in suevite within this drill core (Zhao et al., 2021). We studied the shock metamorphic response of zircon in Chicxulub granitic peak ring rocks to obtain a robust calibration for its use as a shock indicator in non-porous quartzo-feldspathic rocks.

2. Samples and methods

We analyzed 15 thin sections of 14 granitic rock samples from the Expedition 364 drill core (Fig. 1). Using the JEOL JXA 8530F electron microprobe at Arizona State University (ASU), we X-ray mapped these samples and quantitatively identified all zircon grains larger than ca. 20 μ m (Table 1).

Subsequently, we documented all 429 zircon grains in these samples in BSE images to evaluate the prevalence of impactmetamorphic features. Reidite has the same chemical composition

as zircon but is 10% more dense (Kusaba et al., 1985) and consequently shows higher mass contrast in BSE images than zircon with a similar chemical composition. To discriminate ZrSiO₄ from lamellar inclusions with a different composition, we analyzed the chemical compositions of all domains with higher mass contrast with an energy dispersive spectrometer. We then analyzed ZrSiO₄ domains with higher mass contrast in zircon grains with a custombuilt Raman spectrometer at ASU to identify reidite. To quantify the chemical compositions of three ZrSiO₄ grains (Z8, Z13A and Z13B in sample C247_1159.99-1), we used wavelength-dispersive spectrometry with the ASU electron microprobe.

In order to confirm the presence of diagnostic shock metamorphic features, we used EBSD facilities at the John de Laeter Centre at Curtin University in Perth, Australia. Our EBSD analyses characterized shock microtextures in 15 ZrSiO₄ grains in thin section C247_1159.99-1 and 20 ZrSiO₄ grains in thin section C96_748.32. C247 and C96 are core section numbers and 1159.99 and 746.32 are the depths in the drill core in meters below sea floor (mbsf) for these samples; we investigated two thin sections of sample C247_1159.99.

To determine the average shock pressure recorded in quartz, we measured the crystallographic orientations of 131 sets of planar deformation features in 43 quartz crystals in thin section sample C247_1159.99-2 at the University of Vienna, Austria.

§Further analytical details are provided in the Appendix.

3. Results

3.1. Petrographic context

An upper granitic section (747– \sim 1220 mbsf; core sections C95–C266) of the drill core is separated from a deep granitic section (1316–1334 mbsf; core sections C298–C303) by a \sim 60 m thick suevite- and impact melt rock intercalation (Fig. 1) that is part of a \sim 100 m thick imbricate thrust zone between \sim 1220–1316 mbsf (Riller et al., 2018). In contrast to the upper granitic section, the lowermost granitic section between 1316 and 1334 mbsf in the drill core does not show consistent correlations of shock metamorphic features in quartz with the orientation of maximum principal stress σ_1 (Ebert et al., 2020).

Ten samples from core sections C95, C96, C107, C116, C177, C260, C266, C299, C300, and C303 are composed of variably deformed, coarse-grained monzogranite, granodiorite, quartz monzonite, quartz monzodiorite, and monzodiorite, mainly containing cm-size orthoclase, quartz, and albite (Table 1; Fig. A2). Minor phases are mostly chloritized biotite, epidote, magnetite, titanite, and fluorapatite. Zircon typically occurs as a 20 to 40 μm in diameter accessory mineral. The largest coherent zircon grain is 200 μm long and 11 of the 15 zircon grains that are $>100~\mu m$ occur in the three samples from the deepest part of the drill core.

The pre-impact aplite dike in our sample from core section C106 is composed of equant, mm-size feldspar and quartz intergrowths and our sample from core section C230 is from a preimpact pegmatite dike composed of several-cm-size perthitic orthoclase, quartz, and albite crystals; both dike samples C106 and C230 contain minor biotite, epidote, and magnetite, and accessory titanite, zircon, apatite, rutile, and thorite. Two samples from core section C247 are from a fine-grained quartz monzodiorite dike with mm-size intergrowths of quartz, orthoclase, and albite with minor biotite, epidote, magnetite, apatite, allanite, and accessory zircon. The dark grey quartz monzodiorite dike contains inclusions of cm-size feldspar and quartz with irregular sizes and shapes; potassium feldspar inclusions developed 2 mm thick reaction rims of plagioclase with the dike groundmass, suggesting these are wall-rock xenoliths (Morgan et al., 2017). All samples show abundant decorated planar deformation features in quartz

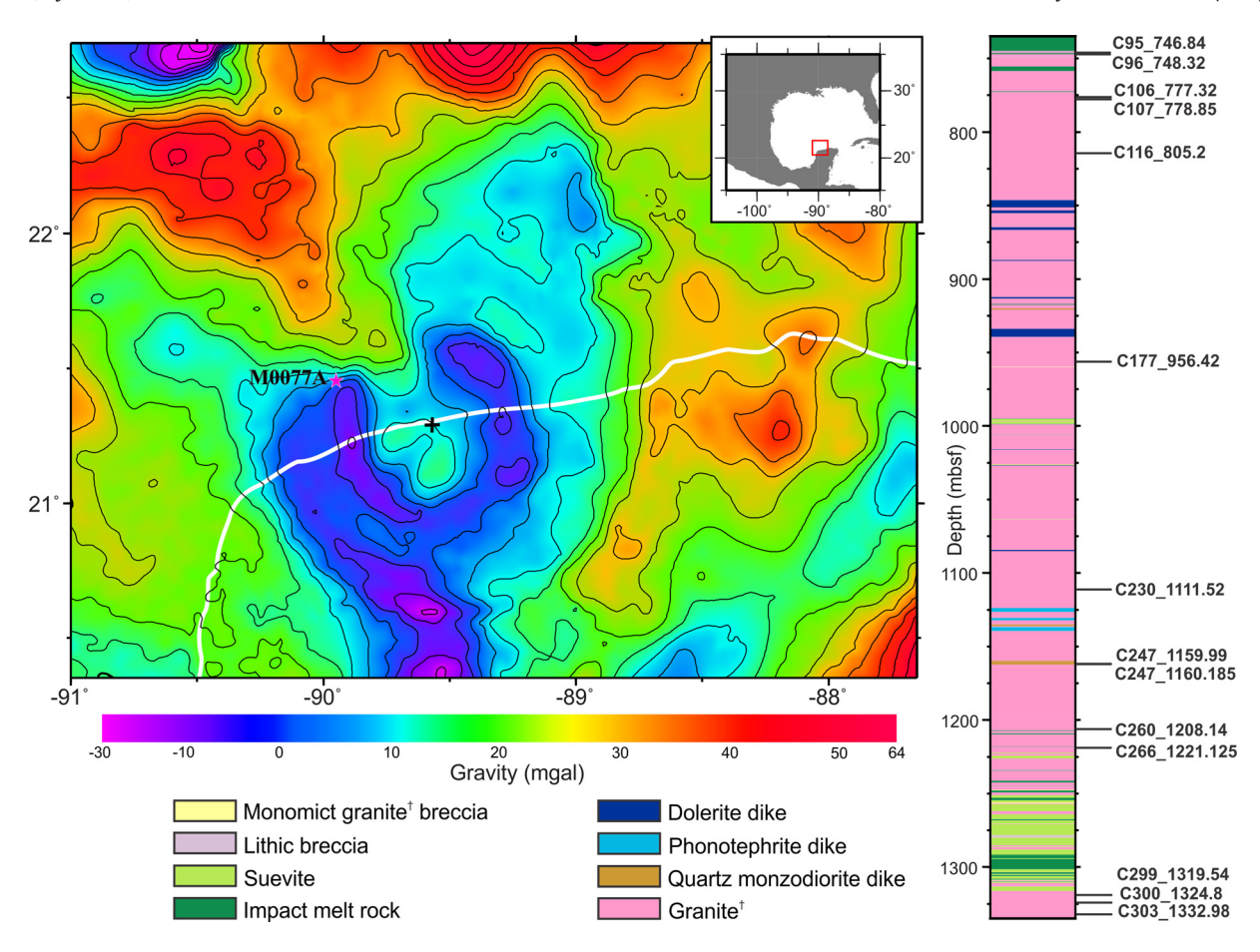


Fig. 1. Location and lithostratigraphy of Expedition 364 Hole M0077A. Gravity anomaly map of the Chicxulub crater after Morgan et al. (2017), modified after Gulick et al. (2013). White line indicates shoreline of the Yucatán peninsula. Pink star marks the offshore location of the Expedition 364 drill site that recovered core M0077A on top of the peak ring, ca. 45 km radial distance from the crater's center (black cross). To the right is a lithostratigraphic sketch of drill core M0077A after Morgan et al. (2017) with sample locations in meters below sea floor (mbsf); † "Granite" is used as a generic term for phaneritic, felsic rocks that include monzogranite, monzodiorite, quartz monzodiorite, quartz monzonite, and granodiorite (Table 1; Fig. A1 and A2). (For interpretation of the colors in the figure(s), the reader is referred to the web version of this article.)

Table 1
Drill core samples from IODP-ICDP Expedition 364, Hole M0077A and deformation types of zircon grains observed in them.

| Core Section | Sub-Section | Depth | Lithology | Zircon grains (n) | | | | | | | |
|--------------|-------------|----------|---------------------------------|-------------------|------------|-----------|------------|-----------|------------------|--|--|
| | | (mbsf) | | sum [†] | undeformed | fractured | brecciated | dispersed | planar fractures | | |
| C95 | 3 | 747.0 | granite/suevite | 25 | 0 | 12 | 11 | 2 | 4 | | |
| C96 | 2 | 748.34 | fractured quartz monzonite | 39 | 0 | 8 | 19 | 12 | 5 | | |
| C106 | 3 | 777.32 | aplite | 12 | 0 | 5 | 5 | 2 | 1 | | |
| C107 | 2 | 778.85 | altered granodiorite | 20 | 1 | 10 | 9 | 0 | 8 | | |
| C116 | 1 | 805.2 | brecciated granodiorite | 33 | 1 | 8 | 24 | 0 | 14 | | |
| C177 | 2 | 956.42 | monzodiorite cataclasite | 31 | 2 | 15 | 6 | 8 | 7 | | |
| C230 | 2 | 1111.52 | pegmatitic quartz monzonite | 5 | 0 | 2 | 3 | 0 | 0 | | |
| C247 | 1 | 1159.99 | quartz monzodiorite dike | 25 | 0 | 12 | 13 | 0 | 9 | | |
| C247 | 1 | 1159.99 | quartz monzodiorite dike | 25 | 0 | 14 | 10 | 1 | 10 | | |
| C247 | 1 | 1160.185 | quartz monzodiorite dike | 30 | 0 | 13 | 5 | 0 | 12 | | |
| C260 | 1 | 1201.3 | quartz monzonite | 42 | 2 | 19 | 21 | 0 | 14 | | |
| C266 | 3 | 1221.125 | quartz monzodiorite cataclasite | 48 | 3 | 21 | 19 | 5 | 10 | | |
| C299 | 1 | 1319.54 | monzogranite | 38 | 2 | 11 | 19 | 6 | 0 | | |
| C300 | 3 | 1324.8 | fractured monzogranite | 29 | 0 | 10 | 15 | 4 | 3 | | |
| C303 | 2 | 1332.98 | fractured monzogranite | 27 | 1 | 21 | 6 | 10 | 1 | | |

[†] Excludes grains with planar fractures because all zircon grains with planar fractures are also fractured or brecciated.

and feldspar, which are not well preserved in feldspar due to pervasive post-impact alteration. Shear planes with mm-size offsets are common. Five samples are brecciated and are, at least in part, cataclasites (Table 1) in which the granitic rock was crushed to mm- and µm-size angular fragments; the quartz monzodiorite dike samples were not affected by cataclasis. Impact melt only occurs in one of the studied samples, C95_747.0, the one close to the upper contact of the granitic peak ring section with a layer of black

impact melt rock. No zircon crystal in the studied samples was in contact with impact melt. Moreover, none exhibit the characteristic granular texture that represents high-temperature recrystallization of decomposed zircon or reidite (Wittmann et al., 2006; Kenny et al., 2017; Timms et al., 2017a; Cavosie et al., 2018). We did not identify characteristic intergrowths of zircon with ZrO₂ that occurs in partly decomposed zircon entrained in impact melt (Timms et al., 2017a, and references therein).

3.2. Deformation features in zircon

We identified 429 zircon crystals in the 15 thin sections (Table 1) that typically occur as single crystals. The apparent sizes of most zircon grains (58%) are 20 to 40 µm, 27% are 40 to 100 µm, 12% are smaller than 20 μm, and only 3% are larger than 100 μm. Of the 429 zircon crystals documented (Table 1), 12 (3%) appear relatively undeformed, 175 (41%) exhibit irregular fractures, 192 (45%) show moderate to severe internal brecciation to anhedral fragments that can be smaller than one um across, and 50 (12%) show comminution and dispersal down to µm-size fragments. Moreover, 98 (23%) of the 429 zircon grains display parallel to sub-parallel, and sometimes bent planar fractures that occur in one to five sets (Fig. 2); 21 of the 98 zircon grains with planar fractures also contain irregular fractures ("fractured" in Table 1), while 77 of these 98 grains are brecciated. Spacing of the planar fractures varies from ca. 1 µm to about 10 µm and their orientations appear to agree with previously characterized crystallographic orientations of planar fractures in zircon along (010), (100), (112), (112), (112), $(\bar{1}\bar{1}2)$, and (011) (Erickson et al., 2013). Not all planar fractures are open, and some with tight spacing resemble feather features in quartz (Ebert et al., 2020; Feignon et al., 2020). Irregular fractures and brecciation sometimes compromised the preservation of planar fractures. Most undeformed zircon grains are small. Fractured zircon grains also tend to be small, but to a lower degree than the undeformed zircon population. Brecciated zircon grains are slightly skewed towards larger grain sizes. Dispersed zircon aggregates show a slight skew towards larger grain sizes with a pronounced overrepresentation among the largest size bin. Sizes of zircon grains with planar fractures show a slight bias towards larger sizes (Table A4).

Planar fractures in zircon grains occur most frequently as two sets; only one zircon grain was found with 5 sets of planar fractures (Fig. A11).

Most zircon occurs as inclusions in plagioclase (35%), biotite (24%), quartz (13%), and potassium feldspar (5%). Allanite, apatite, epidote, Fe-oxide, ilmenite, thorite, and titanite are additional host phases representing 10% of zircon hosts, and 13% of zircon grains occur as components of cataclastic breccias; 18% of the zircon grains occur on grain boundaries and these grains were counted as components hosted by the mineral phase that enclosed the main visible peripheral area of these grains.

One zircon with planar fractures that is hosted by a plagioclase clast in a quartz monzodiorite dike contains ca. 0.5 µmwide lamellar reidite intergrowths. We identified diagnostic Raman bands for reidite at \sim 550, \sim 840, and 880 cm⁻¹ (Fig. 3; van Westrenen et al., 2004) and used EBSD to characterize the crystallographic context for the zircon-reidite intergrowth (Fig. 4). In BSE images (Fig. 4A and C), two sets of reidite lamellae are visible that intersect at a $\sim 45^{\circ}$ angle, based on their relative mass contrast to their zircon host. Only one set of reidite lamellae was identified by EBSD, possibly because the BSE signal is generated from a deeper sample volume than the EBSD data (Reed, 2010), or alternatively. the unindexed lamellae may be locally recessed from the polished surface. Both reidite sets are associated with planar fractures. The minor set of possible reidite lamellae and planar fractures is truncated and offset by the main reidite lamella and its planar fracture set. When plotted on stereonets, the crystallographic data for zircon and reidite display systematic orientation relationships previously described (Erickson et al., 2017; Timms et al., 2017a). Pole clusters for {112}_{reidite} closely align with a {100}_{zircon}, and one set of {112} pole clusters for both phases are also aligned (Fig. 4F). The host zircon in the area of the reidite lamellae records minor $(\sim 5^{\circ})$ cumulative misorientation (Erickson et al., 2017; Timms et al., 2017a).

Table 2 Summary of PDF set abundances and indexed PDF crystallographic orientations determined with the universal stage in quartz grains from thin section C247-2_1159.99-2.

| | Investigated grains [n] | 43 |
|---|------------------------------------|----------------------------|
| | Measured PDF sets [n] | 131 |
| | Measured PDF sets ^a [n] | 124 |
| | Sets/grain [N] | 3.0 |
| | Sets/grain [N*]a | 2.9 |
| | Relative abundance of PDF | sets/grain [%] |
| | 1 set | 4.7 |
| | 2 sets | 20.9 |
| | 3 sets | 44.2 |
| | 4 sets | 25.6 |
| | 5 sets | 4.7 |
| | Total | 100 |
| | Indexed PDF crystallograph | nic orientations; absolute |
| | frequency [%] ^b | |
| | c (0001) | 2.3 |
| | {1014} | 13.7 |
| | $\omega \{10\bar{1}3\}^{c}$ | 61.8 |
| | $\pi \{10\bar{1}2\}$ | 4.6 |
| | r, z {1011} | 1.5 |
| | m {1010} | 0.8 |
| | ξ {1122} | 3.8 |
| | s {1121} | n.d. |
| | ρ {2131} | 2.3 |
| | x {5161} | n.d. |
| | a {1120} | n.d. |
| | {2241} | 2.3 |
| | {3141} | 0.8 |
| | t {4041} | 0.8 |
| | k {5160} | n.d. |
| | Unindexed | 5.3 |
| | Total | 100 |
| _ | | |

^aCalculated only on indexed sets (i.e., unindexed sets excluded). ^bMethod described in Engelhardt and Bertsch (1969). ^cPDFs with measured orientations that plot in the overlapping zone between $\{10\overline{1}4\}$ and $\{10\overline{1}3\}$ were treated as $\{10\overline{1}3\}$. n.d. = none detected.

3.2.1. Quartz monzodiorite dike sample C247_1159.99

To elucidate the petrologic context for the single zirconreidite grain we identified, we present a more detailed description of its occurrence. The host mineral of zircon-reidite grain Z13A in sample C247_1159.99-1 is a 1.2 \times 0.8 mm plagioclase (Ab_{72.1-87.5}An_{11.1-26.2}Or_{0.6-1.8}, n = 12) xenocryst that is entrained in a 2.7 m thick, medium grained, pre-impact quartz monzodiorite dike. We determined an average shock metamorphic overprint for the sample of 17.5 GPa by crystallographic analysis of planar deformation feature (PDF) orientations in quartz crystals (Table 2). This shock pressure constraint is valid for temperatures below the transition to β -quartz at 640 to 650 °C at a pre-impact depth of 8 to 10 km (Shen et al., 1993), which agrees with 185 to 255 °C estimates for the pre-impact temperature regime of the granitic peak ring section (Kring et al., 2020).

We measured the composition of three zircon crystals with the electron microprobe, including the reidite lamella and its host grain Z13A. To avoid damage to the reidite lamella, we used analytical conditions, including a 1 μm -diameter beam, that induce an estimated temperature increase of $\sim\!270\,^{\circ}\text{C}$ in zircon (Reed, 2010). Although we obtained a mixed composition of the reidite lamella and its zircon host, our data suggest a significant enrichment in Al, Ca, and Fe in the reidite-zircon domains compared to other, non-reidite bearing domains in the same zircon host crystal (Table 3).

3.2.2. Shock twins

Two of 15 zircon grains in thin section C247_1159.99-1 contain {112} shock twins (Fig. 5); the reidite-bearing zircon grain does not

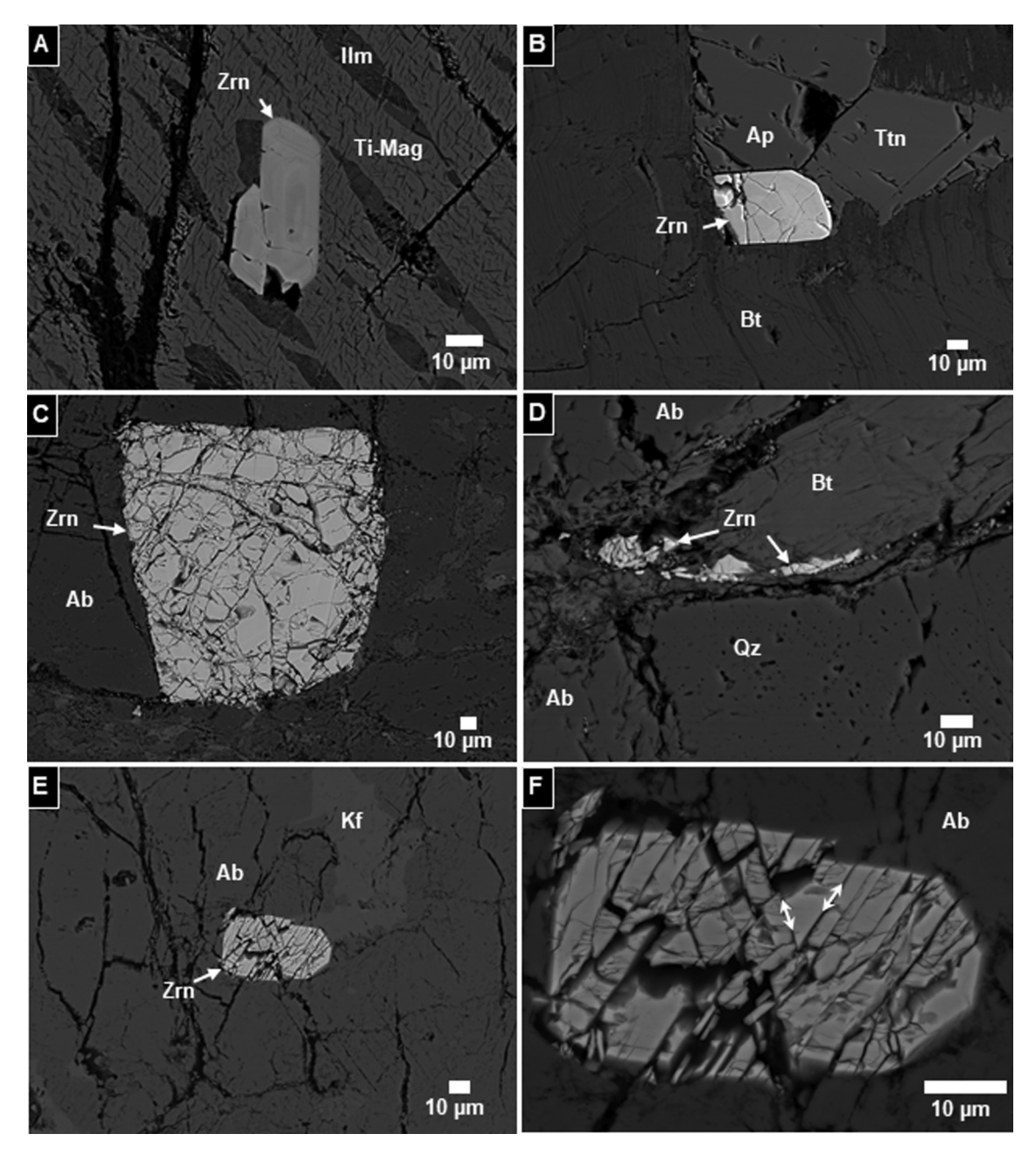


Fig. 2. Backscattered electron images of zircon deformation styles in drill core M0077A. A Apparently undeformed zircon (Zrn) crystal enclosed in titaniferous magnetite (Ti-Mag) that exsolved ilmenite (Ilm) in granite cataclasite sample C266_1221.13. B Fractured zircon crystal associated with biotite (Bt), apatite (Ap), and titanite (Ttn) in quartz-monzodiorite dike sample C247_1160.185. C Brecciated zircon crystal in albite (Ab) in fractured granite sample C300_1324.8, most fractures in this zircon do not extend into its albite host; D Brecciated and dispersed zircon associated with biotite (Bt), albite, and quartz (Qz) in aplite sample C106_777.32. E and F Brecciated zircon crystal with two sets of planar fractures (arrows) in albite crystal with potassium feldspar exsolutions (Kf) in altered granite sample C107_778.85.

display shock-produced mechanical twins. Of the 20 zircon grains we EBSD-mapped in thin section C96_748.52, only one displays a $\{112\}$ shock twin. In agreement with previous studies (e.g., Moser et al., 2011; Erickson et al., 2017), the $\{112\}$ shock twins are misoriented 65° around a <110> axis of the host grain (Fig. 5D).

4. Discussion

4.1. Significance of brittle deformation features in Chicxulub peak ring zircon

Brecciation and dispersion of zircon similar to those in the Chicxulub peak ring were documented in lunar impact breccias (Grange et al., 2013). In terrestrial rocks affected by endogenous deformation, parting along (100) and (111) with sub-planar frac-

ture spacings of several 10s of μm was noted as a characteristic feature of zircon from kimberlites, presumably linked to rapid decompression (Kresten et al., 1975). Planar fractures with spacings of $\sim\!100~\mu m$ in zircon from brecciated lower crustal nepheline pegmatites were interpreted as a result of shock waves associated with explosive volatile release, which may also apply to the parting in kimberlitic zircons (Schaltegger et al., 2015). Less conspicuous, partly healed planar fractures in zircon were reported as single sets from pseudotachylite in an amphibolite-grade shear zone (Kovaleva et al., 2015).

In contrast, crystallographic modeling and observations by Erickson et al. (2013) documented that impact shock-deformed zircon can develop up to 7 sets of planar fractures. Most recently, planar fractures in up to four sets were reported in 16% of zir-

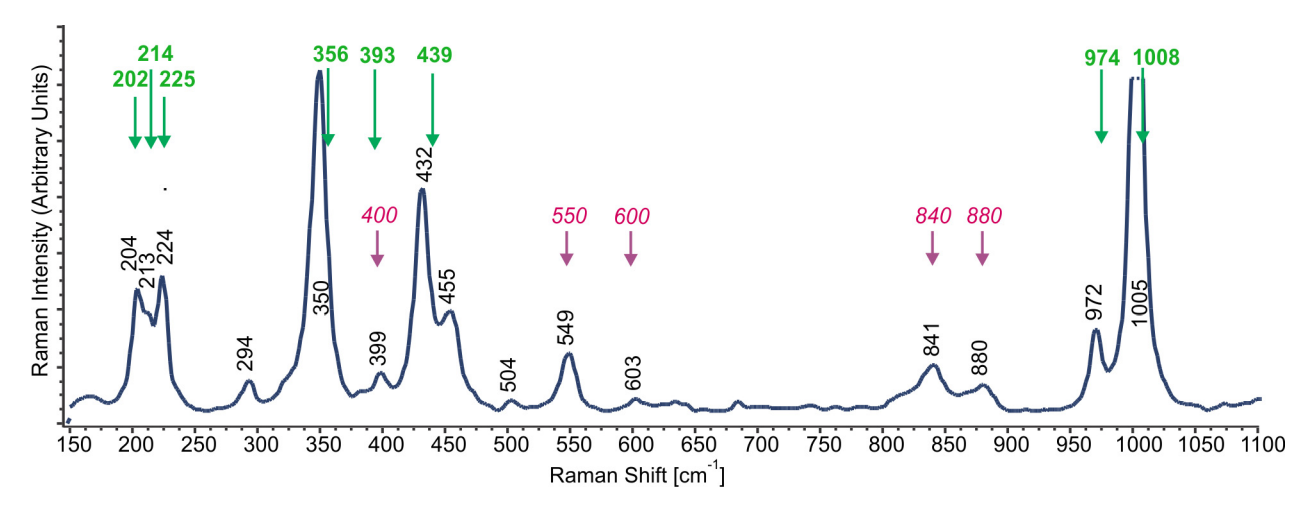


Fig. 3. Raman spectrum of zircon-reidite domain in zircon Z13A of sample C247_1159.99-1. Wavenumbers for prominent Raman bands in the spectrum in black and tilted vertically; bold green wavenumbers are for zircon (Nasdala et al., 2003), italic pink wavenumbers are for reidite (van Westrenen et al., 2004).

Table 3 Electron microprobe data for zircon (zrn) - reidite (red) assemblage in sample C247_1159.99-1.

| • | | , , | , , | | - | | | | | | | |
|-------------------------------------|---------------|---------------|---------------|---------------|---------------|---------------|---------------|---------------|---------------|---------------|---------------|---------------|
| Analysis name [†] | Z13A red a | Z13A red b | Z13A red c | Z13A red d | Z13A zrn e | Z13A zrn f | Z13A zrn g | Z13A zrn h | Z13A zrn i | Z13A zrn j | Z13A zrn k | Z13A zrn l |
| | | | | | | | | | | | | |
| SiO ₂ [wt%] | 33.38 | 33.26 | 32.97 | 33.05 | 33.08 | 32.52 | 33.93 | 33.46 | 34.98 | 33.12 | 32.97 | 33.18 |
| ZrO ₂ [wt%] | 65.39 | 66.63 | 64.98 | 66.22 | 65.49 | 64.70 | 65.23 | 67.67 | 65.35 | 66.29 | 65.92 | 66.01 |
| HfO_2 [wt%] | 0.54 | 0.55 | 0.55 | 0.55 | 0.50 | 0.52 | 0.49 | 0.53 | 0.54 | 0.50 | 0.52 | 0.49 |
| TiO ₂ [wt%] | < 0.04 | < 0.04 | 0.07 | < 0.04 | < 0.04 | 0.06 | 0.05 | 0.05 | 0.06 | 0.07 | < 0.04 | 0.05 |
| UO ₂ [wt%] | 0.10 | < 0.07 | 0.11 | 0.15 | 0.09 | 0.37 | < 0.07 | < 0.07 | 0.19 | < 0.07 | 0.14 | < 0.07 |
| P ₂ O ₅ [wt%] | 0.04 | 0.06 | 0.06 | < 0.03 | 0.05 | 0.06 | 0.05 | < 0.03 | 0.04 | 0.04 | 0.04 | < 0.03 |
| Al_2O_3 [wt%] | 0.10 | 0.14 | 0.14 | 0.09 | < 0.01 | < 0.01 | 0.06 | < 0.01 | 0.28 | < 0.01 | 0.02 | 0.02 |
| $Fe_2O_3*[wt\%]$ | 0.12 | 0.16 | 0.12 | 0.13 | < 0.03 | 0.07 | 0.04 | < 0.03 | 0.06 | < 0.03 | < 0.03 | < 0.03 |
| Y_2O_3 [wt%] | < 0.04 | 0.12 | 0.12 | 0.08 | 0.05 | 0.17 | 0.05 | < 0.04 | < 0.04 | < 0.04 | 0.05 | < 0.04 |
| Er_2O_3 [wt%] | 0.07 | 0.04 | 0.04 | 0.07 | 0.04 | 0.06 | 0.04 | 0.06 | 0.04 | 0.05 | 0.05 | < 0.03 |
| CaO [wt%] | 0.19 | 0.26 | 0.23 | 0.19 | 0.03 | 0.05 | 0.08 | 0.04 | 0.12 | 0.04 | < 0.02 | 0.03 |
| Sum [wt%] | 99.93 | 101.23 | 99.40 | 100.54 | 99.33 | 98.58 | 100.02 | 101.81 | 101.65 | 100.12 | 99.72 | 99.78 |
| Si [afu] | 4.058 | 4.005 | 4.037 | 4.012 | 4.051 | 4.029 | 4.105 | 4.011 | 4.146 | 4.029 | 4.032 | 4.044 |
| Zr [afu] | 3.876 | 3.913 | 3.879 | 3.920 | 3.911 | 3.908 | 3.847 | 3.956 | 3.777 | 3.932 | 3.930 | 3.924 |
| Hf [afu] | 0.019 | 0.019 | 0.019 | 0.019 | 0.017 | 0.018 | 0.017 | 0.018 | 0.018 | 0.017 | 0.018 | 0.017 |
| Ti [afu] | bdl | bdl | 0.006 | bdl | bdl | 0.006 | 0.005 | 0.005 | 0.005 | 0.006 | bdl | 0.004 |
| U [afu] | 0.003 | bdl | 0.003 | 0.004 | 0.003 | 0.010 | bdl | bdl | 0.005 | bdl | 0.004 | bdl |
| P [afu] | 0.004 | 0.007 | 0.007 | bdl | 0.005 | 0.006 | 0.005 | bdl | 0.004 | 0.005 | 0.005 | bdl |
| Al [afu] | 0.014 | 0.019 | 0.021 | 0.013 | bdl | bdl | 0.008 | bdl | 0.039 | bdl | 0.002 | 0.003 |
| Fe [afu] | 0.011 | 0.015 | 0.011 | 0.012 | bdl | 0.007 | 0.003 | bdl | 0.005 | bdl | bdl | bdl |
| Y [afu] | bdl | 0.008 | 0.008 | 0.005 | 0.004 | 0.011 | 0.003 | bdl | bdl | bdl | 0.003 | bdl |
| Er [afu] | 0.003 | 0.001 | 0.002 | 0.003 | 0.002 | 0.002 | 0.002 | 0.002 | 0.001 | 0.002 | 0.002 | bdl |
| Ca [afu] | 0.025 | 0.033 | 0.030 | 0.024 | 0.004 | 0.006 | 0.011 | 0.005 | 0.015 | 0.005 | bdl | 0.004 |
| Sum [afu] | 8.012 | 8.020 | 8.022 | 8.014 | 7.995 | 8.002 | 8.006 | 7.997 | 8.016 | 7.997 | 7.996 | 7.997 |
| - 3111 [414] | 0.0.2 | 0.020 | 5,022 | 5,011 | ,,,,,,, | 0.002 | 0,000 | ,,,,,,, | 0.010 | | | |

 $^{^{\}dagger}$ Analysis names designate reidite (red) domain or zircon (zrn) domain in zircon Z13A and letters a to I correspond to sampling locations in Appendix Fig. A6A. *all Fe as Fe₂O₃; MgO and Dy₂O₃ and Yb₂O₃ were near or below the detection limits (bdl) of 0.01 wt%, 0.03 wt% and 0.03 wt%, respectively; atoms per formula unit [afu] calculated as numbers of ions based on 16 O atoms.

con grains from shatter-coned central peak sandstones of the Spider impact structure in Australia (Cox et al., 2021); quartz shock barometry of the sandstone target rocks indicates average shock pressures of 8 to 10 GPa.

We found that planar fractures occur in 23% of zircon grains in the parautochthonous granitic peak ring rocks from the Chicxulub impact crater that experienced average shock pressures of 17 ± 1 GPa based on quartz shock barometry (Feignon et al., 2020). Moreover, 66% of the zircon grains we studied display several sets of planar fractures (Fig. 2E–F), including planar fractures that are in places associated with shock twins (Fig. 4) and, more rarely, with reidite (Fig. 3). Cross-cutting relationships are hard to establish from the intersecting planar fracture planes. However, their association with reidite that cross-cuts planar fractures (Fig. 4C) indicates some planar fractures formed almost coeval at peak shock pressure, as suggested by Leroux et al. (1999) and Zhao et al. (2021).

Displacement and bending of planar fractures in zircon may relate to shearing and cataclasis in the Chicxulub peak ring during

crater excavation and modification following the passage of the shock wave (Riller et al., 2018), which was estimated to have occurred at pressures between 0.01 to 0.1 GPa (Rae et al., 2019). Some zircon planar fractures may have been reactivated to accommodate shearing during crater modification. However, most planar fractures do not propagate into the zircon host phases (Figs. 2E and F, 5A-D, Appendix Fig. A11), suggesting planar fracture formation with little differential movement. The few zircon crystals that record shear displacements along planar fractures, and the comminuted and dispersed grains that account for ca. 12% of the zircon population studied may record shearing during crater excavation or modification. Other shock-induced planar fractures in granitic Chicxulub peak ring rocks were documented in quartz (Morgan et al., 2016, 2017; Ebert et al., 2020; Feignon et al., 2020; Pittarello et al., 2020), plagioclase (Pittarello et al., 2020), apatite (Cox et al., 2020), titanite (Timms et al., 2019), and in zircon grain separates (Zhao et al., 2021). Different shock metamorphic properties in the granitic rocks of drill core M0077A were proposed by Ebert

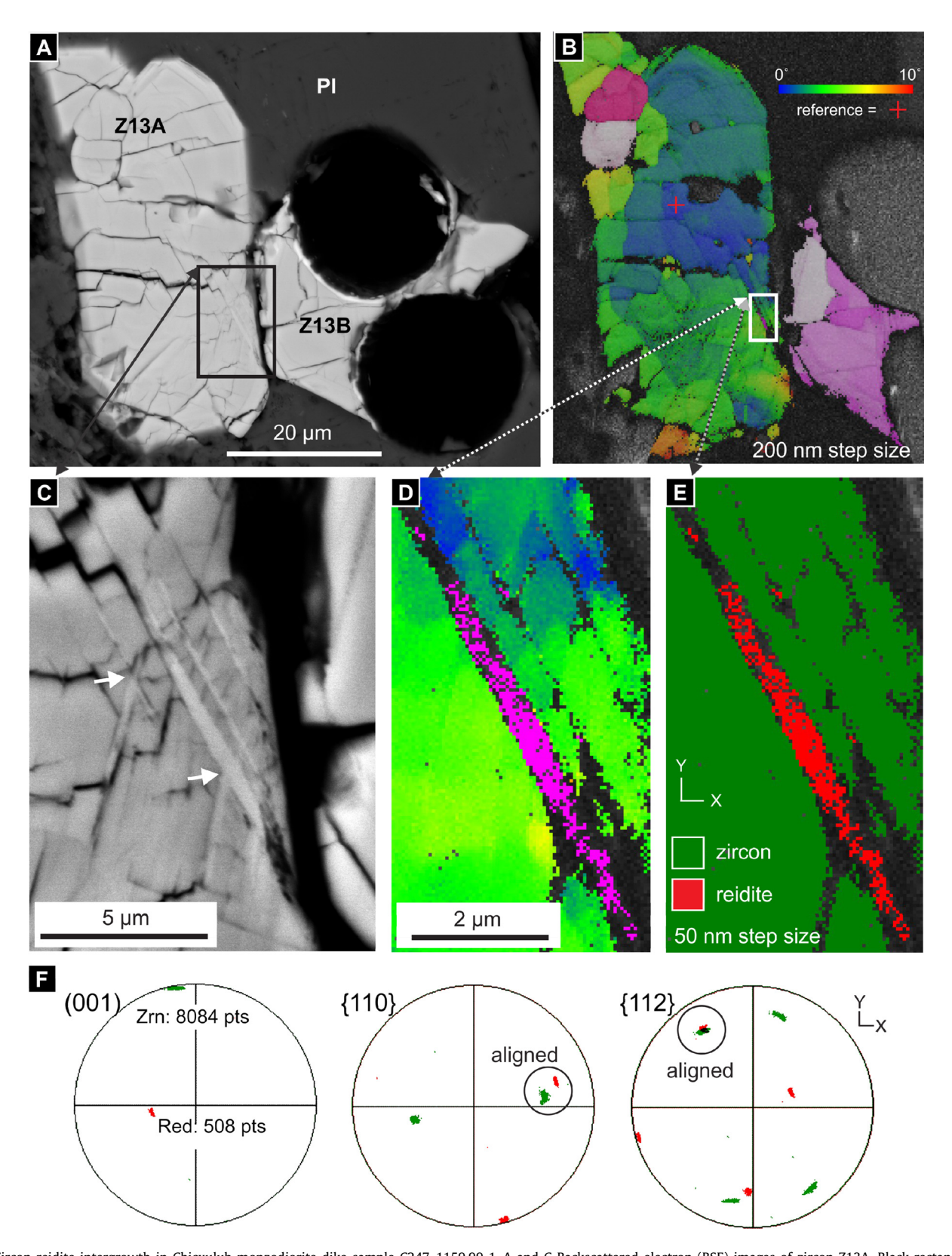


Fig. 4. Zircon-reidite intergrowth in Chicxulub monzodiorite dike sample C247_1159.99-1. A and C Backscattered electron (BSE) images of zircon Z13A. Black rectangle in A indicates location of C; arrows in C indicate intersecting planar fractures and probable reidite lamellae; round, $20 \mu m$ -diameter pits in neighboring zircon grain Z13B are laser ablation inductively-coupled plasma mass spectrometry analysis spots; Pl is plagioclase. B and D Texture component EBSD maps with a cumulative misorientation of 10° . E Phase map showing zircon and reidite lamellae. F Pole figures with crystallographic data shown in E, presented as equal area, lower hemisphere plots in the x/y/z-EBSD map reference frame.

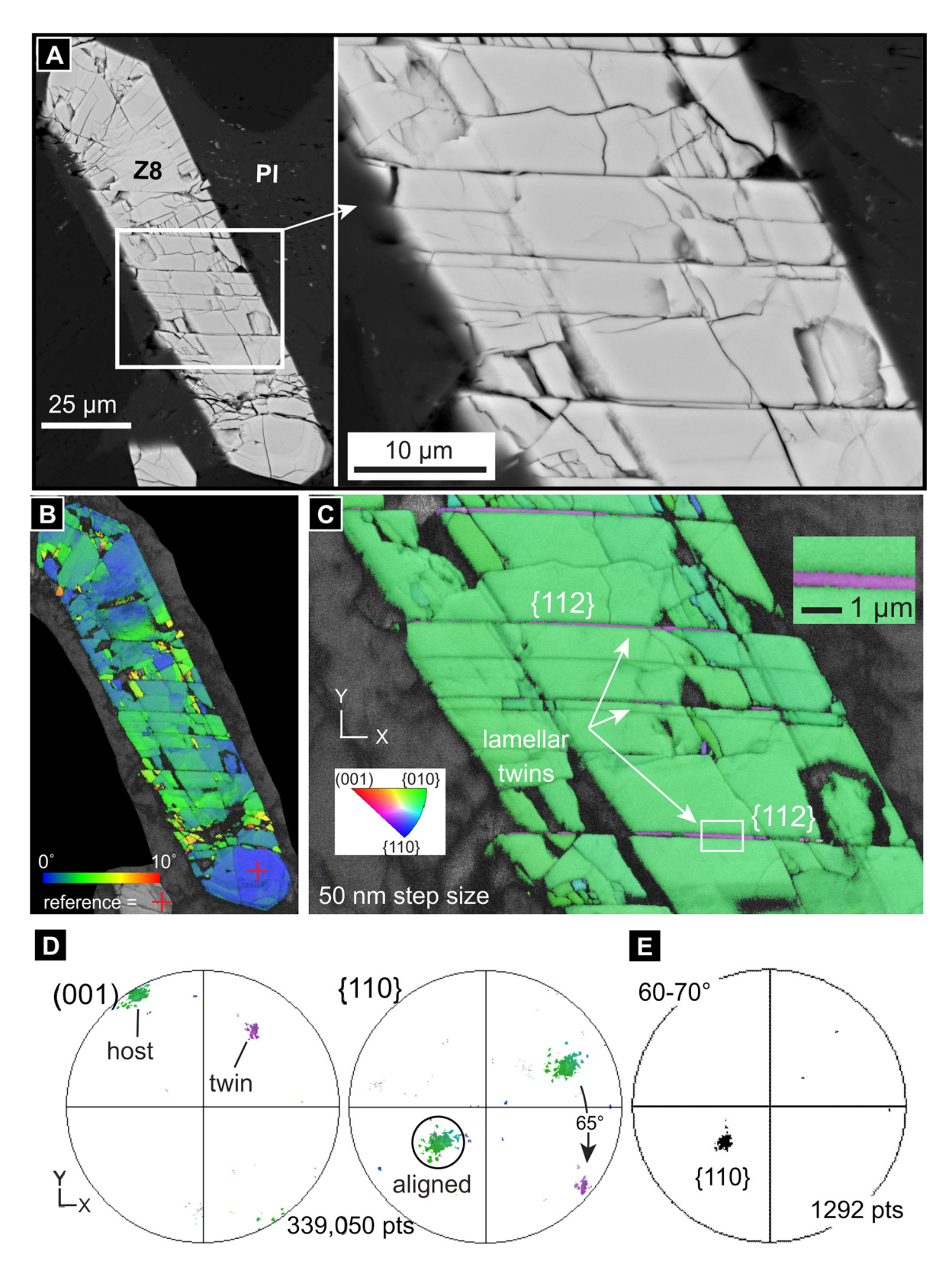


Fig. 5. Shock twins in zircon with planar fractures in Chicxulub quartz-monzodiorite dike sample C247_1159.99-1. A Backscattered electron (BSE) images of zircon Z8; Pl is plagioclase. B Texture component EBSD map with a cumulative misorientation of 10° accommodated by both brittle and crystal-plastic deformation. C Inverted pole figure map illustrating shock twins. D Pole figures with orientation data shown in C, presented as equal area, lower hemisphere plots in the x/y/z-EBSD map reference frame. E Pole figure plot of misorientation axes; note alignment with [110].

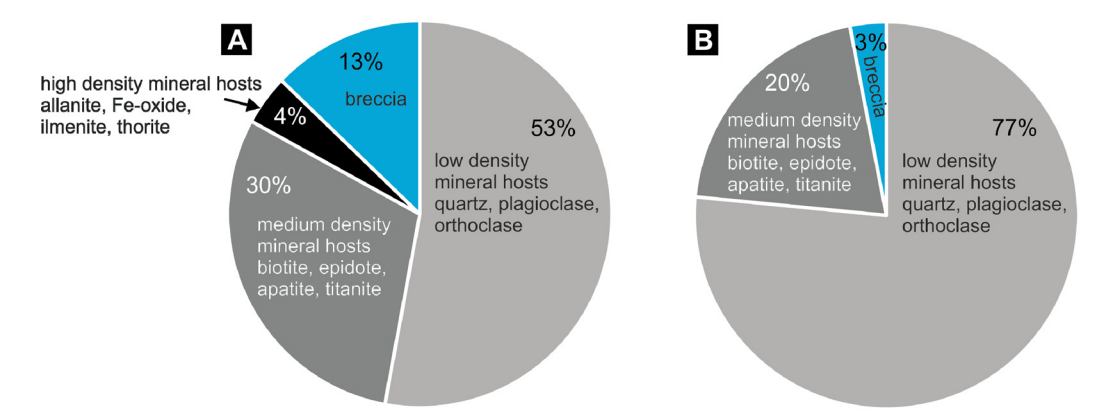


Fig. 6. Chicxulub granitic peak ring zircon mineral hosts. A - Proportions of density-grouped mineral hosts of 429 zircon grains. B - Proportions of density-grouped mineral hosts of a subset from the zircon population in A of 98 zircon grains with planar fractures.

et al. (2020). These authors found similar orientation trends for feather features associated with planar fractures in quartz above an imbricated shear zone that bears impact melt and exotic components, such as gneiss fragments between 1220 and 1316 mbsf in the drilled section (Riller et al., 2018; Fig. 1); chaotic orientations of feather features in quartz occur in granitic rocks within and below that shear zone. Also, Feignon et al. (2020) suggested a slight shock pressure attenuation in the granitic peak ring section with average shock pressures of 17 GPa near the top (752.5 mbsf) and 16 GPa towards the bottom (1311.1 mbsf) based on universal stage analyses of planar deformation features in quartz. While we do not see a clear correlation between the occurrence of zircon with planar fractures and differences in macroscopic deformation features of the samples we analyzed from the drill core, our data show some variation in frequency of occurrence of planar fractures in zircon with depth in the drill core: Only 4% of the 94 zircon grains in the three monzogranite samples (C299_1319.54, C300_1324.8, and C303_1332.98) from a granite block at the bottom of the drill core exhibit planar fractures; this is in contrast to 28% of the 335 zircon grains from the 12 samples in the section above (747.0 to 1221.125 mbsf) displaying planar fractures. In aggregate, this difference may suggest the granite section near the base of the drill core (~1316-1334 mbsf) is decoupled from the upper granitic section (747-~1220 mbsf) as block- and slab-size components of a megabreccia, rather than a continuous section of crater basement (cf., Morgan et al., 2016, 2017; Riller et al., 2018; Rae et al., 2019; Ebert et al., 2020; Feignon et al., 2020).

4.2. Shock impedance and impact metamorphism of zircon

Our comprehensive analysis of petrologic contexts of brittle deformation phenomena indicate that planar fractures correlate with associations of zircon with felsic host minerals of relatively low densities $<3~g/cm^3$ (Fig. 6):

Seventy-five of the 98 zircon crystals with planar fractures (77%) are associated with plagioclase, orthoclase, or quartz, although only 53% (n = 227) of all zircon grains in the samples studied are associated with these low-density mineral phases. In contrast, only 20 of the 98 zircon crystals with planar fractures (20%) are associated with biotite/chlorite, epidote, apatite, or titanite host minerals that have densities of >3 to 3.5 g/cm³, while 30% (n = 128) of all zircon crystals are associated with these medium-density mineral phases. None of the 18 zircon grains enclosed in host crystals with densities >4 g/cm³ (allanite, Fe-oxide, ilmenite, thorite) contain planar fractures, although these high-density mineral phases are associated with 4% of zircon crystals in the samples we studied. Only 3 of the 55 zircon grains that are clasts in monomict breccias devoid of mineral hosts display planar fractures

(3%). A caveat for our samples is that we have to extrapolate the zircon-host relationships to the third dimension in our samples, which was compromised by sample preparation. However, this issue may be minor because of the coarse grain size of most of our samples. To test if the association of hosts of different densities ($<3~g/cm^3$ versus >3 to $3.5~g/cm^3$) with zircon that developed planar fractures is statistically significant, we computed χ^2 tests of independence using the software R (R Core Team, 2020). We obtained a χ^2 value of 11.63 and a probability value of 0.0006, indicating the association of zircon with planar fractures with hosts of low density is significant.

Momentum conservation dictates that a shock wave that encounters the interface between mineral phases of different densities produces reverberated waves that induce lower pressure in the lower density phase and a corresponding wave with higher pressure in the higher density phase. This fundamental principle of shock physics is termed shock impedance, which was described as shock wave velocity times density of the mineral (Stöffler et al., 2018). Hence, if zircon is a higher density phase enclosed in a lower density phase, its higher shock impedance will generate a higher shock pressure than if it was enclosed in a higher density phase. The degree to which shock impedance contrasts affect the development of heterogeneous deformation features in minerals was previously implicated (e.g., Stöffler et al., 1991; Ogilvie et al., 2011; Cox et al., 2020), but has not been rigorously evaluated in natural samples.

Using shock Hugoniot data for zircon and various other minerals and rocks (Ahrens and Johnson, 1995; Marsh, 1980; Mashimo et al., 1983; Trunin et al., 2001), we modeled the shock impedance effect resulting from a shock wave that produced a shock pressure of 17.5 GPa in zircon associated with mineral phases of variable density. For the modeling (Appendix Item 7), we adopted the impedance matching method (Melosh, 1989), which was fundamental for the design of shock recovery experiments (Marsh, 1980; Ahrens and Johnson, 1995; Trunin et al., 2001). This method utilizes the linear relationship between shock and particle velocities in shock Hugoniot data across the regimes of dynamic yielding and phase transitions in specific materials:

$$U = C + S \times u_p,$$

where, U is the shock wave velocity, u_p is the particle velocity, and C and S are constants determined from least squares regression analysis (Melosh, 1989; Ahrens and Johnson, 1995). Our modeling results reveal a power-law correlation between the shock impedance amplified pressure P_i exerted on a zircon inclusion and the density of its host materials ρ_h :

$$P_i = 39 \times \rho_h^{-0.507}$$

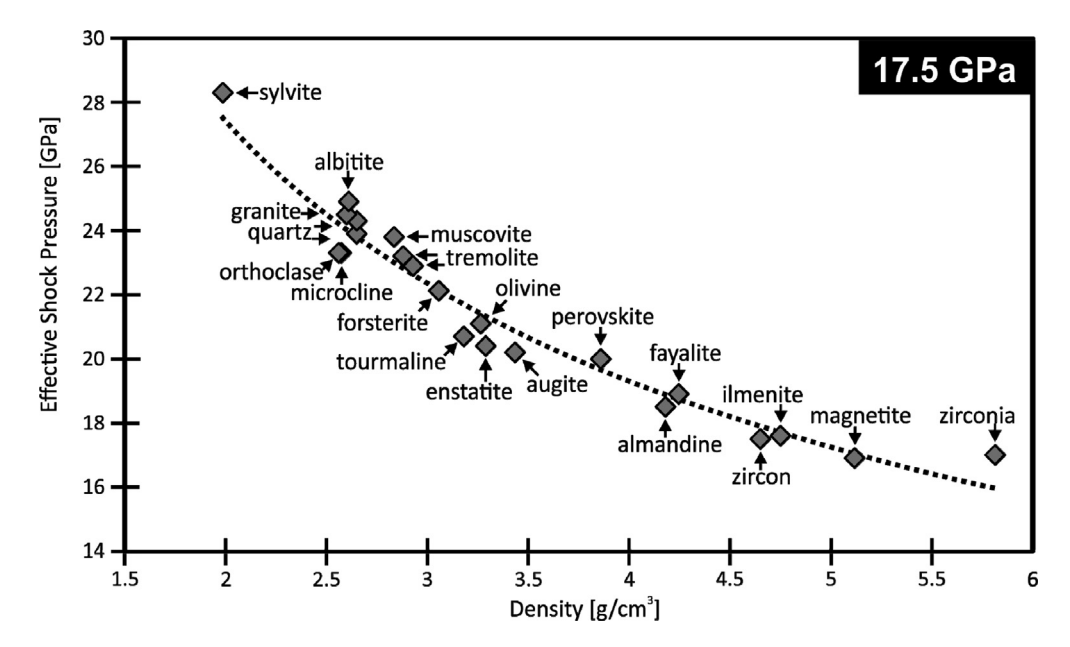


Fig. 7. Shock impedance effect on zircon inclusions in mineral hosts that experience a shock pressure of 17.5 GPa. Diagram shows shock pressures exerted on zircon inclusions in various mineral phases and rocks based on linear shock-particle velocity relations. Shock Hugoniot data are from Marsh (1980), Mashimo et al. (1983), Ahrens and Johnson (1995), Trunin et al. (2001), and references therein. The trend line illustrates a power law relationship ($y = 39x^{-0.507}$; $R^2 = 0.96$) between the shock-impedance amplified pressure exerted on a 4.65 g/cm³ zircon inclusion and the density of host materials that experience 17.5 GPa shock pressure. Two density-shock pressure relationships for quartz and tremolite were calculated from independently determined shock Hugoniot data.

Uncertainties for the modeled shock-impedance amplified pressures are estimated to be on the order of ± 1 GPa, mainly due to error propagation from measurement uncertainties of the shock Hugoniot data. This relationship is useful to illustrate the difference in shock impedance experienced by zircon depending on its petrologic context. In absence of shock Hugoniot data for biotite and apatite, the power-law correlation between the shock impedance amplified pressure experienced by a zircon inclusion and the density of its host material, and its graphical depiction in Fig. 7 allow us to extrapolate the shock impedance effect for these potential zircon hosts. It follows that in our samples, the effect of shock impedance on zircon enclosed in felsic minerals and rocks with densities of ~ 2.6 g/cm³ that experience a shock pressure of 17.5 GPa results in an amplified shock pressure of up to 24 \pm 1 GPa in zircon. In contrast, zircon enclosed in biotite, apatite, epidote, or titanite with densities of 3 to 3.5 g/cm³ that experienced an average shock pressure of 17.5 GPa were only exposed to an amplified shock pressure of up to 21 \pm 1 GPa. Zircon enclosed in mineral phases with densities >4 g/cm³ that were exposed to shock pressures of 17.5 GPa experienced only minor shock impedance amplified pressures <20 GPa.

Hence, the preferential incidence of shock-related planar fracturing in zircon hosted by low density minerals documented in this study is likely a function of shock impedance. Whereas quartzbased shock barometry determined an average shock metamorphic overprint between 16 and 18 GPa for the granitic host rocks of zircon that exhibits planar fractures in 23% of all grains studied (Feignon et al., 2020), their petrologic contexts suggest that these planar fractures developed in significant abundance in zircon grains that experienced shock pressures >20 GPa - if shock impedance is considered. A quantitative evaluation of the occurrence of planar fractures in quartz, plagioclase, apatite, and titanite in granitic Chicxulub peak ring rocks (Morgan et al., 2016, 2017; Ebert et al., 2020; Feignon et al., 2020; Pittarello et al., 2020; Cox et al., 2020; Timms et al., 2019) similar to our analysis of zircon could calibrate planar fractures as diagnostic shock pressure indicators in granitic rocks.

4.3. Implications for the formation mechanism of reidite

The transformation of zircon to reidite is thought to involve a displacive deformation of the zircon lattice to obtain the 10% denser reidite lattice (Kusaba et al., 1985). This proposed process was challenged by recent theoretical considerations that suggest the symmetry elements in zircon and reidite are too different to allow for a displacive transformation (Stangarone et al., 2019). Instead, Stangarone et al. (2019) favor a reconstructive transformation that includes crystallization of reidite from a non-quenchable, high-pressure-low-symmetry (HPLS) zircon polymorph. However, crystallization of reidite from a HPLS polymorph is at odds with the rapid and complete transformation of zircon to reidite in shock recovery experiments at ambient pre-shock temperatures (Kusaba et al., 1985; Fiske et al., 1994; Leroux et al., 1999; Erickson et al., 2020). Our compositional data for a zircon-reidite domain from the Chicxulub crater (Table 3) also contrast with electron microprobe data for a ZrSiO₄ grain from an ejecta layer of the Chesapeake Bay impact. This grain was mostly transformed to reidite and did not reveal consistent enrichments in impurities (Glass et al., 2002), which may be due to different transformation mechanisms operating on these reidite grains. Cavosie et al. (2021) recently investigated a ZrSiO₄ grain similar to the one analyzed by Glass et al. (2002) and found large-scale transformation to reidite occurred via shearing to lamellar reidite followed by epitaxial growth of dendritic reidite. We did not observe evidence for impact melting or other indicators for high temperatures that could have accommodated the reconstructive growth of reidite in the petrologic context of Z13A.

Impurities in natural zircon are thought to hinder transition kinetics, effectively stabilizing impurity-rich zircon at higher pressure than pure zircon (van Westrenen et al., 2004). However, the zircon-reidite domain in our Chicxulub sample is distinctly enriched in elements that are impurities in the zircon lattice, such as CaO, Al₂O₃, and FeO (Table 3). These impurities could be evidence for post-impact alteration along fractures and grain boundaries, even though no epidote occurs in the immediate vicinity of reiditebearing zircon grain Z13A (Fig. 4), and analytical totals suggest the analyzed zircon-reidite volumes did not contain significant void

space (Table 3). Alternatively, Montalvo et al. (2019) showed that certain trace elements (Y, Al, Mg, Mn, Ca, Ti, and Be) are enriched along reidite-zircon grain boundaries, which these authors linked to the martensitic transformation of zircon to reidite coupled with short-range diffusion. The 1300 ppm U associated with the reiditezircon domain in Z13A (Table 3) may have been an additional factor accommodating shear-induced transformation to reidite. While metamictization is thought to impede the transformation of zircon to reidite (e.g., van Westrenen et al., 2004; Wittmann et al., 2006; Erickson et al., 2017), the granitic peak ring rocks were located at a pre-impact depth of 8 to 10 km, where they experienced a thermal regime that allowed auto-annealing and prevented the accumulation of radiation damage and metamictization (Rasmussen et al., 2019). However, because high actinide contents are non-unique to grain Z13A in the Chicxulub granitic peak-ring rocks (Appendix Tables A2 and A3), additional factors must have been at work to produce reidite lamellae in zircon grain Z13A. As pointed out by Stöffler et al. (1991), a perpendicular orientation of a grain boundary of zircon-reidite Z13A and the lower density host plagioclase to the shock front would have generated the most pronounced shearing and impedance contrast-related pressure excursion. It is somewhat difficult to reconstruct this geometric relationship from the cutting plane that exposes zircon-reidite grain Z13A, because the domain that shows the reidite lamella abuts a fractured zircon grain. This contact relationship is not unique, as at least ten zircon assemblages among the 429 zircon grains described herein show similar abutting with neighboring zircon grains (e.g., Fig. 2A, Fig. A7A-C), yet no reidite is associated with these assemblages. Hence, the onset of reidite formation in the parautochthonous granitic rocks from the Chicxulub impact structure appears to be a product of multiple factors that may include certain levels of impurities, shock impedance contrasts, and crystallographic orientation towards the shock front.

4.4. Onset of zircon-to-reidite transformation in natural impactites

Based on shock experiments, the onset of the transition of zircon to its high-pressure polymorph reidite occurs between 20 to 30 GPa. Some shock recovery experiments report small amounts of reidite (ca. 1 vol.%) at shock pressures of 20 GPa (Fiske et al., 1994; Erickson et al., 2020), while other studies suggest less than 5% of experimentally shocked zircon transformed to reidite at 30 GPa (Kusaba et al., 1985). Our study unambiguously shows that very small amounts of reidite occur in rocks that experienced an average shock pressure of 16 to 18 GPa at a pre-impact depth of 8 to 10 km (Morgan et al., 2016). However, considering the petrologic context for the zircon-reidite grain that we identified in the Chicxulub granitic peak ring rocks (Fig. 4), the shock-impedance amplified pressure this zircon grain experienced could have been as high as 25 GPa (Fig. 7). In fact, a significant portion of zircon grains in the Chicxulub granitic peak ring rocks must have experienced shock-impedance amplified pressures in excess of 20 GPa (Fig. 7), as the average pressure recorded by quartz was 17 \pm 1 GPa (Feignon et al., 2020).

We cannot rule out that we might have missed small domains of reidite in the 429 zircon grains surveyed with BSE images. However, the mass contrast due to the 10% higher density of reidite than zircon instills confidence that we did not miss significant occurrences of reidite. Previous EBSD analyses of zircon grains in the Chicxulub granitic lower peak ring drill core section confirm our observation that reidite is rare in the granitic rock section of the Chicxulub peak ring:

 Timms et al. (2019) report EBSD data for eight zircon grains in granitic samples from 814.85 mbsf and 1030 mbsf that do not contain diagnostic shock features.

- Cox et al. (2020) report one zircon grain from a granite sample at 1050.1 mbsf with a single, small {112} shock twin lamella; overall, these authors analyzed five zircon grains from granitic samples in the lower peak ring section with EBSD, none of which contained reidite.
- Zhao et al. (2021) produced grain separates from 6 samples of Chicxulub peak ring granitoids and conducted EBSD measurements on 6 of their zircon grains from a sample depth of 979.33 mbsf, detecting shock twins in two of these zircon grains.
- We found that shock twinning occurs in three of the 35 zircon grains we investigated by EBSD in samples from depths of 748.52 mbsf (Appendix Fig. A10) and 1159.99 mbsf (Fig. 5 and A9).

Experimental constraints suggest such mechanical twins may start to form in zircon at 11 GPa (Morozova et al., 2018) and deformation twins were shown to result from high strain rates (Christian and Mahajan, 1995). Because strain rates are at a maximum during shock compression, the nucleation of microtwins in zircon should occur in this deformation regime (Rae et al., 2019). While we did not quantitatively determine the incidence of shock twins in our samples, these twins obviously formed in association with planar fractures (Figs. 5, A9, A10). This association may be due to the high shear stresses that occur near the tips of rapidly expanding cracks, which generate stress rates that favor twinning (Christian and Mahajan, 1995). However, in metallic alloys, shock twins are known to increase in volume fraction with increasing grain size and critical twinning pressures also depend on stacking-fault free energy (Murr and Esquivel, 2004). These formation conditions for shock twinning likely also apply to zircon. Our study found that planar fractures are more robust quantitative shock indicators than shock twins in the typically small zircon grains of the granitic Chicxulub peak ring rocks that experienced onset conditions for the transformation to reidite.

5. Conclusions

In a comprehensive, in situ study of deformation features in zircon, we surveyed 429 zircon grains in 14 drill core samples of parautochthonous granitic rocks from the peak ring of the Chicxulub impact structure. These rocks are thought to have been located at a pre-impact depth of 8 to 10 km. Previously, average shock pressures for these rocks were constrained to 17 \pm 1 GPa based on quartz shock-barometry, which suggests conditions close to the onset for the transition of zircon to its high-pressure polymorph reidite (Fiske et al., 1994; van Westrenen et al., 2004; Morozova et al., 2018; Erickson et al., 2020). We observed one zircon-reidite intergrowth in BSE images of 429 zircon grains studied, and identified shock twins in 3 of 35 zircon grains studied by EBSD. The most common impact metamorphic effect we observed in zircon is shock-induced planar fracturing. Planar fractures commonly occur in multiple directions, preferentially in zircon enclosed in low density host minerals, as a manifestation of the amplification of pressure due to shock impedance differences. Using impedance matching modeling, we quantified the amplification of shock pressure due to impedance contrasts in minerals with different densities associated with zircon. Our modeling indicates that due to shock impedance differences, zircon enclosed in minerals of low density, such as quartz or feldspar, could have experienced amplified shock pressures up to 25 GPa in the Chicxulub samples. This amplification decreases and becomes unrecognizable in mineral phases that have densities close to zircon, which is recorded by the decrease of incidence of zircon grains with planar fractures associated with such medium and higher density mineral hosts.

For the shock pressure calibration of zircon, our study shows the importance of accounting for petrologic contexts before assigning shock pressure constraints. This is especially important for accessory minerals that are frequently associated with mineral hosts of high impedance contrast. In this context, the rare occurrence of reidite in the Chicxulub parautochthonous granitic peak ring rocks may be due to shock impedance contrasts, certain levels of impurities, and crystallographic orientation towards the shock front, which point to formation closer to the maximum shock impedance amplified 25 GPa than the 17.5 GPa indicated by quartz shock barometry.

CRediT authorship contribution statement

Axel Wittmann: Conceptualization, Methodology, Formal Analysis, Writing-Original draft preparation, Visualization, Investigation, Data Curation, Resources; Aaron J. Cavosie: Conceptualization, Methodology, Formal Analysis, Writing-Original draft preparation, Visualization, Investigation, Resources; Nicholas E. Timms: Conceptualization, Methodology, Formal Analysis, Writing-Original draft preparation, Visualization, Investigation; Ludovic Ferrière: Conceptualization, Methodology, Formal Analysis, Writing-Original draft preparation, Visualization, Investigation, Resources; Auriol Rae: Conceptualization, Methodology, Visualization, Writing - Original draft preparation, Review & Editing; Cornelia Rasmussen: Writing - Review & Editing; Catherine Ross: Writing - Review & Editing; Daniel Stockli: Writing - Review & Editing; Martin Schmieder: Writing - Review & Editing; David A. Kring: Writing - Review & Editing; Michael Poelchau: Writing - Review & Editing; Long Xiao: Writing - Review & Editing; Jiawei Zhao: Writing - Review & Editing; Joanna V. Morgan: Funding acquisition, Project administration, Supervision, Writing - Review & Editing; Sean P.S. Gulick: Funding acquisition, Project administration, Writing - Review & Editing, Supervision; and the IODP-ICDP Expedition 364 Scientists: Writing -Review & Editing, Resources.

Declaration of competing interest

The authors declare that they have no known competing financial interests or personal relationships that could have appeared to influence the work reported in this paper.

Acknowledgements

This study is dedicated to Jay Melosh. We thank captain and crew, drilling team, and technical staff who participated in shipboard and/or shore-based operations for IODP-ICDP Expedition 364. The European Consortium for Ocean Research Drilling (ECORD) implemented Expedition 364 with funding from the International Ocean Discovery Program (IODP) and the International Continental Scientific Drilling Program (ICDP). The Yucatán State Government and Universidad Nacional Autónoma de México provided logistical support. We thank reviewers Gavin Kenny and Elizaveta Kovaleva and editor William McKinnon for the peerreview of this manuscript. Data and samples can be requested from IODP. The contribution of AW was supported by the U.S. Science Support Program grant OCE 14-50528 and NSF grant OCE 1737087, the contributions of DK by NSF grant OCE 1736826, and the contributions of SG, CR, CR, DS by NSF grant OCE 1757351. Support to AJC was provided by the Space Science and Technology Centre and the John de Laeter Centre at Curtin University. Sonia Boyum for calculating the χ^2 tests. This LPI Contribution #2639. This is University of Texas Institute for Geophysics Contribution #5040 and Center for Planetary Systems Habitability Contribution #0037. The IODP-ICDP Expedition 364 Science Party is S. Gulick (US), J. V. Morgan (UK), G. Carter (UK), E. Chenot (France), G. Christeson (US), Ph. Claeys (Belgium), C. Cockell (UK), M. J. L. Coolen (Australia), L. Ferrière (Austria), C. Gebhardt (Germany), K. Goto (Japan), H. Jones (US), D. A. Kring (US), J. Lofi (France), C. Lowery (US), R. Ocampo-Torres (France), L. Perez-Cruz (Mexico), A. Pickersgill (UK), M. Poelchau (Germany), A. Rae (UK), C. Rasmussen (US), M. Rebolledo-Vieyra (Mexico), U. Riller (Germany), H. Sato (Japan), J. Smit (Netherlands), S. Tikoo (US), N. Tomioka (Japan), M. Whalen (US), A. Wittmann (US), J. Urrutia-Fucugauchi (Mexico), L. Xiao (China), and K. E. Yamaguchi (Japan); post-expedition associated scientists include S. Goderis (Belgium), P. Kaskes (Belgium), F. Schulte (Germany), G. Osinski (Canada), R. Grieve (Canada), N. Artemieva (Russia), T. Bralower (USA), J. Zhao (China).

Appendix A. Supplementary material

Supplementary material related to this article can be found online at https://doi.org/10.1016/j.epsl.2021.117201.

References

- Ahrens, T.J., Johnson, M.L., 1995. Shock wave data for minerals. In: Ahrens, T.J. (Ed.), Mineral Physics and Crystallography, A Handbook of Physical Constants. American Geophysical Union, Washington, D.C., pp. 143–183.
- Cavosie, A.J., Timms, N.A., Ferrière, L., Rochette, P., 2018. FRIGN zircon-the only terrestrial mineral diagnostic of high-pressure and high-temperature shock deformation. Geology 46 (10), 891–894.
- Cavosie, A.J., Biren, M.B., Hodges, K.V., Wartho, J.-A., Horton Jr., J.W., Koeberl, C., 2021. Dendritic reidite from the Chesapeake Bay impact horizon, Ocean Drilling Program Site 1073 (offshore northeastern USA): a fingerprint of distal ejecta? Geology 49 (2), 201–205. https://doi.org/10.1130/G47860.1.
- Chen, D.-L., Zhang, A.-C., Pang, R.-L., Chen, J.-N., Li, Y., 2019. Shock-induced phase transformation of anorthitic plagioclase in the eucrite meteorite Northwest Africa 2650. Meteorit. Planet. Sci. 54 (7), 1548–1562.
- Christian, J.W., Mahajan, S., 1995. Deformation twinning. Prog. Mater. Sci. 39, 1–157.Cox, M.A., Cavosie, A.J., Bland, P.A., Miljkovic, K., Wingate, M.T.D., 2018. Microstructural dynamics of central uplifts: reidite offset by zircon twins at the Woodleigh impact structure, Australia. Geology 46 (11), 983–986.
- Cox, M.A., Erickson, T.M., Schmieder, M., Christoffersen, R., Ross, D.K., Cavosie, A.J., Bland, P.A., Kring, D.A., IODP-ICDP Expedition 364 Scientists, 2020. High-resolution microstructural and compositional analyses of shock deformed apatite from the peak ring of the Chicxulub Impact Crater. Meteorit. Planet. Sci. 55 (8), 1715–1733.
- Cox, M.A., Cavosie, A.J., Poelchau, M.H., Kenkmann, T., Miljković, K., Bland, P.A., 2021.
 Asymmetric shock deformation at the Spider impact structure, Western Australia. Meteorit. Planet. Sci. 56 (2), 331–351. https://doi.org/10.1111/maps.13621.
- Ebert, M., Poelchau, M.H., Kenkmann, T., Schuster, B., 2020. Tracing shock-wave propagation in the Chicxulub crater: implications for the formation of peak rings. Geology 48, 814–818.
- Engelhardt, W.v., Bertsch, W., 1969. Shock induced planar deformation structures in quartz from the Ries crater, Germany. Contrib. Mineral. Petrol. 20, 203–234.
- Erickson, T.M., Cavosie, A.J., Moser, D.E., Barker, I.R., Radovan, H.A., 2013. Correlating planar microstructures in shocked zircon from the Vredefort Dome at multiple scales: crystallographic modeling, external and internal imaging, and EBSD structural analysis. Am. Mineral. 98, 53–65. https://doi.org/10.2138/am. 2013.4165.
- Erickson, T.M., Pearce, M.A., Reddy, S.M., Timms, N.E., Cavosie, A.J., Bourdet, J., Rickardt, W.D.A., Nemchin, A.A., 2017. Microstructural constraints on the mechanisms of the transformation to reidite in naturally shocked zircon. Contrib. Mineral. Petrol. 172 (6), 26. https://doi.org/10.1007/s00410-016-1322-0.
- Erickson, T.M., Cline, C.J., Jakubek, R., Cintala, M.J., Timms, N.E., 2020. Shock deformation in zircon, a comparison of results from shock-reverberation and single-shock experiments. In: Lunar and Planetary Science Conference. abstract #1581.
- Feignon, J.-G., Ferrière, L., Leroux, H., Koeberl, C., 2020. Characterization of shocked quartz grains from Chicxulub peak ring granites and shock pressure estimates. Meteorit. Planet. Sci. 10, 2206–2223. https://doi.org/10.1111/maps.13570.
- Fiske, P.S., Nellis, W.J., Sinha, A.K., 1994. Shock-induced phase transitions of ZrSiO₄, reversion kinetics, and implications for terrestrial impact craters (abstract). Eos 75, 416–417.
- Glass, B.P., Liu, S., Leavens, P., 2002. Reidite: an impact-produced high-pressure polymorph of zircon in marine sediments. Am. Mineral. 87, 562–565.
- Grange, M.L., Pidgeon, R.T., Nemchin, A.A., Timms, N.E., Meyer, C., 2013. Interpreting U-Pb data from primary and secondary features in lunar zircon. Geochim. Cosmochim. Acta 101, 112–132.
- Gulick, S.P.S., Christeson, G.L., Barton, P.J., Grieve, R.A.F., Morgan, J.V., Urrutia-Fucugauchi, J., 2013. Geophysical characterization of the Chicxulub impact crater. Rev. Geophys. 51, 31–52. https://doi.org/10.1002/rog.20007.

- Kenny, G.G., Morales, L.F., Whitehouse, M.J., Petrus, J.A., Kamber, B.S., 2017. The formation of large neoblasts in shocked zircon and their utility in dating impacts. Geology 45 (11), 1003–1006.
- Kovaleva, E., Klötzli, U., Habler, G., Wheeler, U., 2015. Planar microstructures in zircon from paleo-seismic zones. Am. Mineral, 100, 1834–1847.
- Kresten, P., Fels, P., Berggren, G., 1975. Kimberlitic zircons a possible aid in prospecting for kimberlites. Miner. Depos. 10, 47–56.
- Kring, D.A., Tikoo, S.M., Schmieder, M., Riller, U., Rebolledo-Vieyra, M., Simpson, S.L., Osinski, G.R., Gattacceca, J., Wittmann, A., Verhagen, C.M., Cockell, C.S., Coolen, M.J.L., Longstaffe, F.J., Gulick, S.P.S., Morgan, J.V., Bralower, T.J., Chenot, E., Christeson, G.L., Claeys, P., Ferrière, L., Gebhardt, C., Goto, K., Green, S.L., Jones, H., Lofi, J., Lowery, C.M., Ocampo-Torres, R., Perez-Cruz, L., Pickersgill, A.E., Poelchau, M.H., Rae, A.S.P., Rasmussen, C., Sato, H., Smit, J., Tomioka, N., Urrutia-Fucugauchi, J., Whalen, M.T., Xiao, L., Yamaguchi, K.E., 2020. Probing the hydrothermal system of the Chicxulub impact crater. Sci. Adv. 6 (22), eaaz3053. https://doi.org/10.1126/sciadv.aaz3053.
- Kusaba, K., Syono, Y., Kikuchi, M., Fukuoka, K., 1985. Shock behavior of zircon: phase transitions to scheelite structure and decomposition. Earth Planet. Sci. Lett. 72, 433–439.
- Leroux, H., Reimold, W.U., Koeberl, C., Hornemann, U., Doukhan, J.-C., 1999. Experimental shock deformation in zircon: a transmission electron microscopic study. Earth Planet. Sci. Lett. 169, 291–301.
- Lounejeva, E., Ostroumov, M., Sánchez-Rubio, G., 2002. Micro-Raman and optical identification of coesite in suevite from Chicxulub. In: Koeberl, C., MacLeod, K.G. (Eds.), Catastrophic Events and Mass Extinctions: Impacts and Beyond. Geological Society of America, Boulder, Colorado, pp. 47–54.
- Marsh, S.P., 1980. LASL Shock Hugoniot Data. University of California Press, Berkeley and Los Angeles, p. 658.
- Mashimo, T., Nagayama, K., Sawaoka, A., 1983. Shock compression of zirconia ZrO₂ and zircon ZrSiO₄ in the pressure range up to 150 GPa. Phys. Chem. Miner. 9, 237–247.
- Melosh, H.J., 1989. Impact Cratering A Geologic Process. Oxford Monographs on Geology and Geophysics, vol. 11. Oxford University Press, Oxford, p. 245.
- Montalvo, S.D., Reddy, S.M., Saxey, D.W., Rickard, W.D.A., Fougerouse, D., Quadir, Z., Johnson, T.E., 2019. Nanoscale constraints on the shock-induced transformation of zircon to reidite. Chem. Geol. 507, 85–95. https://doi.org/10.1016/j.chemgeo. 2018.12.039.
- Morgan, J.V., Gulick, S.P.S., Bralower, T.J., Chenot, E., Christeson, G.L., Claeys, P.F., Cockell, C.S., Collins, G.S., Coolen, M., Ferrière, L., Gebhardt, C., Goto, K., Jones, H., Kring, D.A., Le Ber, E., Lofi, J., Long, X., Lowery, C., Mellett, C., Ocampo-Torres, R., Osinski, G.R., Perez-Cruz, L.L., Pickersgill, A., Poelchau, M., Rae, A., Rasmussen, C., Rebolledo-Vieyra, M., Riller, U.P., Sato, H., Schmitt, D.R., Smit, J., Tikoo, S., Tomioka, N., Urrutia Fucugauchi, J., Whalen, M.T., Wittmann, A., Yamaguchi, K.E., Zylberman, W., 2016. The formation of peak rings in large impact craters. Science 354 (6314), 878–882.
- Morgan, J.V., Gulick, S.P.S., Mellett, C.L., Green, S.L., the Expedition 364 Scientists, 2017. Chicxulub: drilling the K-Pg Impact Crater. In: Proceedings of the International Ocean Discovery Program. International Ocean Discovery Program, p. 176.
- Morozova, I., Shieh, S.R., Moser, D.E., Barker, I.R., Hanchar, J.M., 2018. Strength and deformation of zircon at crustal and mantle pressures. In: Moser, D.E., Corfu, F., Darling, J.R., Reddy, S.E., Tait, K. (Eds.), Microstructural Geochronology: Planetary Records down to Atom Scale. John Wiley & Sons, pp. 169–182.
- Moser, D.E., Cupelli, C.L., Barker, I.R., Flowers, R.M., Bowman, J.R., Wooden, J., Hart, J.R., 2011. New zircon shock phenomena and their use for dating and reconstruction of large impact structures revealed by electron nanobeam (EBSD, CL, EDS) and isotopic U-Pb and (U-Th)/He analysis of the Vredefort dome. Can. J. Earth Sci. 48. 117–139.
- Murr, L.E., Esquivel, E.V., 2004. Observations of common microstructural issues associated with dynamic deformation phenomena: twins, microbands, grain size effects, shear bands, and dynamic recrystallization. J. Mater. Sci. 39, 1153–1168. https://doi.org/10.1023/B:JMSC.0000013870.09241.c0.
- Nasdala, L., Zhang, M., Kempe, U., Panczer, G., Gaft, M., Andrut, M., Plötze, M., 2003. Spectroscopic methods applied to zircon. In: Hanchar, J.M., Hoskin, P.W.O. (Eds.), Zircon. Mineralogical Society of America, Washington, D.C., pp. 427–467.
- Ogilvie, P., Gibson, R.L., Reimold, W.U., Deutsch, A., Hornemann, U., 2011. Experimental investigation of shock metamorphic effects in a metapelitic granulite: the importance of shock impedance contrast between components. Meteorit. Planet. Sci. 46 (10), 1565–1586.
- Pittarello, L., Ferrière, L., Feignon, J.-G., Osinski, G.R., Koeberl, C., 2020. Preferred orientation distribution of shock-induced planar microstructures in quartz and feldspar. Meteorit. Planet. Sci. 55 (5), 1082–1092. https://doi.org/10.1111/maps. 13490
- R Core Team, 2020. R: A Language and Environment for Statistical Computing. R Foundation for Statistical Computing, Vienna, Austria. https://www.R-project.org/.

- Rae, A.S.P., Collins, G.S., Poelchau, M.H., Riller, U.P., Davison, T.M., Grieve, R.A.F., Osinski, G.R., Morgan, J.V., Gulick, S.P.S., Chenot, E., Christeson, G.L., Claeys, P., Cockell, C.S., Coolen, M.J.L., Ferrière, L., Gebhardt, C., Goto, K., Green, S., Jones, H., Kring, D.A., Lofi, J., Lowery, C.M., Ocampo-Torres, R., Perez-Cruz, L., Pickersgill, A.E., Rasmussen, C., Rebolledo-Vieyra, M., Sato, H., Smit, J., Tikoo, S.M., Tomioka, N., Urrutia-Fucugauchi, J., Whalen, M.T., Wittmann, A., Xiao, L., Yamaguchi, K., 2019. Stress-strain evolution during peak-ring formation: a case study of the Chicxulub impact structure. J. Geophys. Res., Planets 124. https://doi.org/10.1029/2018/E005821.
- Rasmussen, C., Stockli, D.F., Ross, C.H., Pickersgill, A., Gulick, S.P.S., Schmieder, M., Christeson, G.L., Wittmann, A., Kring, D.A., Morgan, J.V., the IODP-ICDP Expedition 364 Science Party, 2019. U-Pb memory behavior in Chicxulub's peak ring applying U-Pb depth profiling to shocked zircon. Chem. Geol. 525, 356–367.
- Reed, S.J.B., 2010. Electron Microprobe Analysis and Scanning Electron Microscopy in Geology. Cambridge University Press, Cambridge, p. 189.
- Riller, U.P., Poelchau, M.H., Rae, A.S.P., Schulte, F.M., Melosh, H.J., Collins, G.S., Grieve, R.A.F., Morgan, J.V., Gulick, S.P.S., Lofi, J., Diaw, A., McCall, N., Kring, D.A., Green, S.L., Chenot, E., Christeson, G.L., Claeys, P., Cockell, C.S., Coolen, M.J.L., Ferrière, L., Gebhardt, C., Goto, K., Jones, H., Xiao, L., Lowery, C.M., Ocampo-Torres, R., Perez-Cruz, L., Pickersgill, A.E., Rasmussen, C., Rebolledo-Vieyra, M., Sato, H., Smit, J., Tikoo-Schantz, S.M., Tomioka, N., Whalen, M.T., Wittmann, A., Yamaguchi, K., Urrutia-Fucugauchi, J., Bralower, T.J., 2018. Rock fluidization during peak-ring formation of large impact structures. Nature 562, 511–518.
- Schaltegger, U., Ulianov, A., Müntener, O., Ovtcharova, M., Peytcheva, I., Vonlanthen, P., Vennemann, T., Antognini, M., Girlanda, F., 2015. Megacrystic zircon with planar fractures in miaskite-type nepheline pegmatites formed at high pressures in the lower crust (Ivrea Zone, southern Alps, Switzerland). Am. Mineral. 100, 83–94.
- Shen, A.H., Bassett, W.A., Chou, I., 1993. The α - β quartz transition at high temperatures and pressures in a diamond-anvil cell by laser interferometry. Am. Mineral, 78, 694–698.
- Stangarone, C., Angel, R.J., Prencipe, M., Mihailova, B., Alvaro, M., 2019. New insights into the zircon-reidite phase transition. Am. Mineral. 104, 830–837.
- Stöffler, D., Keil, K., Scott, E.R.D., 1991. Shock metamorphism of ordinary chondrites. Geochim. Cosmochim. Acta 55, 3845–3867.
- Stöffler, D., Hamann, C., Metzler, K., 2018. Shock metamorphism of planetary silicate rocks and sediments: proposal for an updated classification system. Meteorit. Planet. Sci. 53 (1), 5–49.
- Timms, N.E., Erickson, T.M., Pearce, M.A., Cavosie, A.J., Schmieder, M., Tohver, E., Reddy, M.A., Zanetti, M.R., Nemchin, A.A., Wittmann, A., 2017a. A pressure-temperature phase diagram for zircon at extreme conditions. Earth-Sci. Rev. 165, 202
- Timms, N.E., Erickson, T.M., Zanetti, M.R., Pearce, M.A., Cayron, C., Cavosie, A.J., Reddy, M.A., Wittmann, A., Carpenter, P.K., 2017b. Cubic zirconia in >2370°C impact melt records Earth's hottest crust. Earth Planet. Sci. Lett. 477, 52–58.
- Timms, N.E., Pearce, M.A., Erickson, T.M., Cavosie, A.J., Rae, A.S.P., Wheeler, J., Wittmann, A., Ferrière, L., Poelchau, M.H., Tomioka, N., Collins, G.S., Gulick, S.P.S., Rasmussen, C., Morgan, J.V., IODP-ICDP Expedition 364 Scientists, 2019. New shock microstructures in titanite (CaTiSiO₅) from the peak ring of the Chicxulub impact structure, Mexico. Contrib. Mineral. Petrol. 174, 38. https://doi.org/10.1007/s00410-019-1565-7.
- Trunin, R.F., Gudarenko, L.F., Zhernokletov, M.V., Simakov, G.V., 2001. Experimental Data on Shock Compression and Adiabatic Expansion of Condensed Matter. Russian Federal Nuclear Center, Sarov, p. 446.
- van Westrenen, W., Frank, M.R., Hanchar, J.M., Fei, Y., Finch, R.J., Zha, C.-S., 2004. In situ determination of the compressibility of synthetic pure zircon (ZrSiO₄) and the onset of the zircon-reidite phase transition. Am. Mineral. 89, 197–203.
- Wittmann, A., Kenkmann, T., Schmitt, R.T., Stöffler, D., 2006. Shock metamorphosed zircon in terrestrial impact craters. Meteorit. Planet. Sci. 41, 433–454.
- Xing, W., Lin, Y., Zhang, C., Zhang, M., Hu, S., Hofmann, B.A., Sekine, T., Xiao, L., Gu, L., 2020. Discovery of reidite in the lunar meteorite Sayh al Uhaymir 169. Geophys. Res. Lett. 47, e2020GL089583. https://doi.org/10.1029/2020GL089583.
- Zhao, J., Xiao, L., Gulick, S.P.S., Morgan, J.V., Kring, D., Urrutia Fucugauchi, J., Schmieder, M., de Graaff, S.J., Wittmann, A., Ross, C.H., Claeys, P., Pickersgill, A., Kaskes, P., Goderis, S., Rasmussen, C., Vajda, V., Ferriere, L., Feignon, J.-G., Chenot, E., Perez-Cruz, L., Sato, H., Yamaguchi, K., IODP-ICDP 364 scientists, 2020. Geochemistry, geochronology and petrogenesis of Maya Block granifoids and dikes from the Chicxulub Impact Crater, Gulf of México: Implications for the assembly of Pangea. Gondwana Res. 82, 128–150. https://doi.org/10.1016/j.gr.2019.12.003.
- Zhao, J., Xiao, L., Xiao, Z., Morgan, J.V., Osinski, G.R., Neal, C.R., Gulick, S.P.S., Riller, U., Claeys, P., Zhao, S., Prieur, N.C., Nemchin, A., Yu, S., IODP 364 Science Party, 2021. Shock-deformed zircon from the Chicxulub impact crater and implications for cratering process. Geology. https://doi.org/10.1130/G48278.1.